

See discussions, stats, and author profiles for this publication at: <https://www.researchgate.net/publication/231651288>

# Synthesis and Ethanol Sensing Properties of Self-Assembled Monocrystalline ZnO Nanorod Bundles by Poly(ethylene glycol)-Assisted Hydrothermal Process

ARTICLE in THE JOURNAL OF PHYSICAL CHEMISTRY C · FEBRUARY 2009

Impact Factor: 4.77 · DOI: 10.1021/jp8082166

CITATIONS

67

READS

25

4 AUTHORS, INCLUDING:



Zeng Yi

Jilin University

47 PUBLICATIONS 1,297 CITATIONS

SEE PROFILE



Tong Zhang

chemical

160 PUBLICATIONS 2,540 CITATIONS

SEE PROFILE



Wang Rui

Chongqing University

276 PUBLICATIONS 1,962 CITATIONS

SEE PROFILE

Article

**Synthesis and Ethanol Sensing Properties of  
Self-Assembled Monocrystalline ZnO Nanorod Bundles  
by Poly(ethylene glycol)-Assisted Hydrothermal Process**

Yi Zeng, Tong Zhang, Lijie Wang, Rui Wang, Wuyou Fu, and Haibin Yang

*J. Phys. Chem. C*, **2009**, 113 (9), 3442-3448 • DOI: 10.1021/jp8082166 • Publication Date (Web): 09 February 2009

Downloaded from <http://pubs.acs.org> on March 8, 2009

**More About This Article**

Additional resources and features associated with this article are available within the HTML version:

- Supporting Information
- Access to high resolution figures
- Links to articles and content related to this article
- Copyright permission to reproduce figures and/or text from this article

[View the Full Text HTML](#)



**ACS Publications**  
High quality. High impact.

The Journal of Physical Chemistry C is published by the American Chemical Society, 1155 Sixteenth Street N.W., Washington, DC 20036

# Synthesis and Ethanol Sensing Properties of Self-Assembled Monocrystalline ZnO Nanorod Bundles by Poly(ethylene glycol)-Assisted Hydrothermal Process

Yi Zeng, Tong Zhang,\* Lijie Wang, and Rui Wang

State Key Laboratory on Integrated Optoelectronics, College of Electronic Science and Engineering, Jilin University, Changchun 130012, People's Republic of China

Wuyou Fu and Haibin Yang

State Key Laboratory of Superhard Materials, Jilin University, Changchun 130012, People's Republic of China

Received: September 15, 2008; Revised Manuscript Received: December 27, 2008

The flowerlike ZnO nanorod bundles, consisting of closely packed nanorods with diameter of  $\sim 90$  nm, have been successfully synthesized by a poly(ethylene glycol) (PEG)-assisted hydrothermal route at low temperature (80 °C). The results characterized from FESEM, TEM, and SAED demonstrate that the nanorod structures are single crystals and formed from self-assembled nanoparticles. Further investigation of the formation mechanism reveals that the PEG-assisted hydrothermal process is vital to the formation of the complex nanostructures. The sensors based on the ZnO nanostructures exhibit excellent ethanol-sensing properties at reduced working temperature (250 °C), which could still respond to 1 ppm ethanol. The sensitivity of the sensor to 100 ppm ethanol is about 154.3 with the response time of 12 s. The enhancement in sensing properties of the present ZnO sensor may be attributed to the peculiar ZnO nanostructures.

## 1. Introduction

Highly sensitive and reliable gas sensors are very important to many applications for monitoring poisonous and hazardous gases for environmental and security purposes in domestic and industrial areas. The recognition of the gas-sensing capability of a semiconducting oxide can date back to the 1960s when it was observed that the adsorption of reducing gas on metal oxides could result in a change in the electrical conductivity of the oxides,<sup>1</sup> and this phenomenon quickly led to extensive practical applications of gas sensors. Among semiconducting oxide gas sensors, zinc oxide (ZnO) is a well-known n-type II–VI semiconducting oxide with a direct band gap of 3.37 eV and a large exciton binding energy of 60 meV.<sup>2</sup> Due to its unique conductance properties, it is one of the most promising candidates toward miniaturized and highly sensitive chemical sensors, which have been widely reported for the detection of different oxidizing and reducing gases, such as O<sub>2</sub>, CO, NH<sub>3</sub>, and H<sub>2</sub>.<sup>3–7</sup> Although the general principle of the sensing mechanism is appreciated, there are still problems concerned with achieving selectivity and sensitivity. It is well-known that various approaches have been introduced to improve these problems, including adjustment of the microstructure, change of the preparation method, and addition of catalysts/dopants.<sup>8–10</sup> As far as the gas-sensing application is concerned, nanoscaled ZnO provides many advantages, such as having higher surface-to-volume ratio, and exhibiting increasing sensitivity and lower operating temperature.

Nanocrystalline ZnO with various exciting morphologies have been prepared by various techniques, such as thermal evaporation, chemical vapor deposition (CVD), template-assisted growth, and electrochemical process.<sup>11–15</sup> However, for most of these methods, vacuum technique, high temperature, catalysts,

or noxious gas compounds may be required, which will increase the cost and limit the choice of substrates.<sup>16</sup> In contrast, the solution methods are potentially suitable for scale-up due to their low growth temperature, low cost, and facile manipulation. Hydrothermal synthesis, as an important method of solution synthesis, has been proven to be a versatile approach for preparation of ZnO due to the convenience and simplicity in the fabrication. Recently, Feng et al. have synthesized flowerlike ZnO nanostructures in ethanol solution by the hydroethylene-diamine-assisted hydrothermal method for the gas detection of ethanol.<sup>17</sup> Zhang et al. have prepared flowerlike ZnO nanostructures by cetyltrimethylammonium bromide-assisted hydrothermal process at low temperature (120 °C).<sup>18</sup> In addition, Wang et al. have developed a hydrothermal route on a Si wafer sputtered with a thin ZnO film for the synthesis of vertical ZnO nanorod arrays which exhibit enhanced sensitivity toward NH<sub>3</sub>.<sup>19</sup> Further investigation of low-temperature fabrication is deemed necessary for low cost sensors with good sensing characteristics at low operating temperature.

Herein, we present a simple hydrothermal route to the fabrication of flowerlike ZnO nanorod bundles at low temperature (80 °C). The crystallinity, structure, and morphology of the present ZnO are characterized, and the corresponding formation mechanism has been preliminarily discussed. Ethanol sensor based on the flowerlike ZnO nanorod bundles is fabricated, which shows high sensitivity and fast reversible response to ethanol due to the large surface-to-volume ratio. The sensing mechanism of the nanocrystalline ZnO has also been primarily discussed. It is believed that the flowerlike ZnO nanorod bundles are very promising in fabricating high-performance gas sensors.

## 2. Experimental Procedures

All the chemicals, purchased from Beijing Chemicals Co. Ltd., were analytic grade reagents and used without further

\* To whom correspondence should be addressed. Tel.: +86-431-85168385. Fax: +86-431-85168417. E-mail: zhangtong@jlu.edu.cn.

purification. Deionized water with a resistivity of 18.0 M $\Omega$  cm was used in all experiments. The typical experiment details are described as follows: 50 mL of aqueous solution of zinc acetate dihydrate (0.25 M) and 0.1 g of poly(ethylene glycol) (PEG,  $M_w = 10\,000$ ) were mixed together and kept with mild magnetic stirring for 10 min. Then, 1 M ammonia (NH<sub>4</sub>OH) was slowly added dropwise into the above solution under vigorous stirring until it resulted in a white aqueous solution and pH = 8.0. The final aqueous solution was transferred into a Teflon-lined stainless steel autoclave, sealed tightly, and treated hydrothermally at 80 °C for 20 h. Subsequently, the autoclave was cooled down naturally. The precipitates were centrifuged and then washed with absolute ethyl alcohol and deionized water for 3 times prior to drying in air at 60 °C for further characterization.

The phase purity of the obtained samples was characterized by X-ray powder diffraction (XRD, Rigaku D/max-Ra) with graphite monochromatized and Cu K $\alpha$ ,  $\lambda = 0.154\,18$  nm. Field emission scanning electron microscopy (FESEM) images were obtained on a JEOL JSM-6700F microscope operated at 5 kV, and the energy-dispersive X-ray spectrometry (EDX) result was measured by the FESEM attachment. Transmission electron microscopy (TEM) images, selected area electron diffraction (SAED) pattern, and high-resolution transmission electron microscopy (HRTEM) images were obtained on a Hitachi H-8100 microscope operated at 200 kV and a JEOL JEM-3010 microscope operated at 200 kV, respectively. Raman-scattering spectrum was measured by HR-800 LabRam confocal Raman microscope with a backscattering configuration made by JY Co. in France, excited by the 514 nm line of an argon ion laser at room temperature. Room temperature photoluminescence (PL) and UV–vis spectra were recorded on HR-800 LabRam Infinity spectrophotometer excited by a continuous He–Cd laser with the excitation wavelength of 325 nm and UV-3150 spectrophotometer, respectively. The surface area of the ZnO products was measured based on the principle of N<sub>2</sub> sorption with a Micromeritics ASAP 2020 M Brunauer–Emmett–Teller (BET) surface analyzer.

The present products were mixed with deionized water in a weight ratio of 100:25 to form a paste. The sensors were obtained by coating the paste onto the ceramic tube on which a pair of gold electrodes were previously printed, and then a Ni–Cr heating wire was inserted into the tube to form a side-heated gas sensor. The details of the sensor fabrication were similar to those reported in other literature.<sup>20</sup>

The gas sensing properties were measured by the gas sensing measurement system of RQ1 intelligent test meter (Qingdao, China). The sensor response was defined as the ratio ( $S = R_a/R_g$ ) of the resistance of the sensor in dry air ( $R_a$ ) to that in target gases ( $R_g$ ). The operating temperature of the sensor was varied between 200 and 350 °C. The response and recovery time were defined as the time taken by the sensor to achieve 90% of the total resistance change in the case of adsorption and desorption, respectively.

### 3. Results and Discussion

**Structure and Morphology.** Figure 1 displays the typical XRD pattern obtained from the as-prepared products. All of the diffraction peaks can be well indexed to pure wurtzite structure of ZnO with lattice constants of  $a = 3.249$  Å,  $c = 5.206$  Å, which are consistent with the values in the standard card (JCPDS No. 36-1451). No diffraction peaks from any other impurities are detected.

Figure 2 shows the morphological and structural characterizations of the ZnO products. A typical FESEM image of an

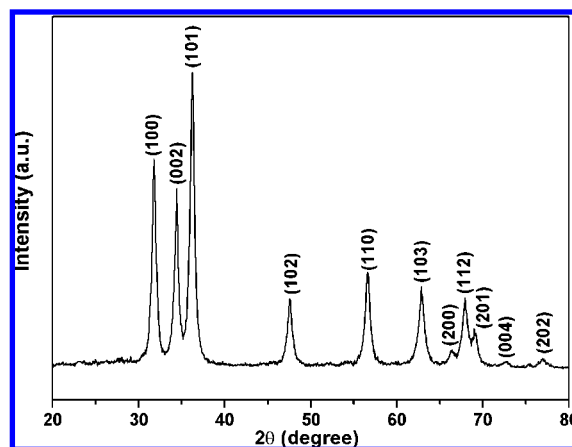
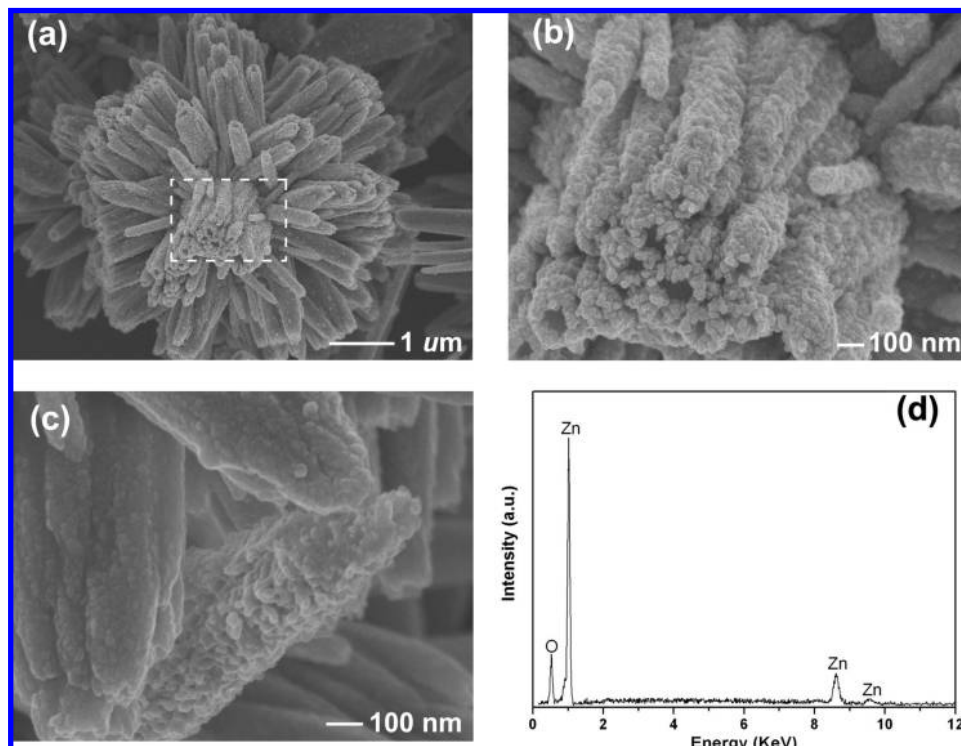


Figure 1. XRD pattern of the as-prepared products.

individual ZnO nanostructure is shown in Figure 2a. It can be clearly seen that flowerlike ZnO structure is composed of many closely packed nanorods of about 90 nm in diameter and 1.2  $\mu$ m in length, which appear to extend radially from the center with very rough surfaces. Part of the nanorods tend to parallel-arrange tightly and show an obvious trend to attach to each other. The magnified FESEM images in Figure 2b,c show the detailed morphologies of the ZnO nanorod bundles. Apparently, rough and particle-assembled surfaces of each ZnO nanorods are exhibited. The nanoparticles serving as building blocks are tightly packed in rodlike shape with the diameter of about 20 nm. It can be concluded that these nanorods are formed from the attachment of ZnO nanoparticles and further gather into bundles from the active sites in various directions. It is also observed that there are craterlets on the top of the nanorods, which look like the formation of nanotubes. The EDX result shown in Figure 2d demonstrates that the present ZnO contains only Zn and O, and the atomic ratio of Zn and O is about 50.65:49.35.

To further obtain the structural information of the ZnO products, typical TEM and HRTEM images are recorded, as shown in Figure 3. Figure 3a reveals the TEM image of the whole flowerlike shape of an individual ZnO nanorods bundle. The result shows that ZnO nanorods have diameter in the range of 50–280 nm and length of 1–1.5  $\mu$ m, which is similar to that shown in Figure 2. It also shows that the ends of the nanorods have relatively smaller diameters compared with that of the middle parts. The enlarged images of the area marked with white rectangles are shown in Figure 3b,c, in which it is observed that particle-composed nanorods have very rough surfaces. It is noteworthy that the rodlike structures are sufficiently stable, which cannot be destroyed even after ultrasonication for a long time. The inset of Figure 3c shows the corresponding SAED pattern taken from the nanorod. The diffraction pattern, composed of many separate spots, could be indexed to a single-crystal structure with the growth direction along the ZnO nanorod [0001] ( $c$  axis). It is interesting and surprising that the assembled rodlike structure composed of many nanoparticles exhibits an almost single-crystalline diffraction pattern, which should be attributed to the aggregated nanoparticles that compose the ZnO nanorod and array along the [0001] crystallographic direction. The typical HRTEM image of the tip region in a ZnO nanorod is shown in Figure 3d. The spacing between adjacent lattice planes is about 0.26 nm, which corresponds to the distance between two (0002) crystal planes of hexagonal ZnO. The HRTEM image also shows the Moiré stripes, which could result from two crystallites with slightly



**Figure 2.** Morphological and structural characterizations of the as-prepared ZnO products: (a) a low-magnification FESEM image; (b, c) high-magnification FESEM images; and (d) the EDX result of the present ZnO.

different orientation. In the self-assembled process, it is energetically favored that the adjacently primary nanoparticles tend to rotate to share the same 3D crystallographic orientation and further coalesce among each other due to reducing the interfacial energy of the whole nanorod system. But in this process, the stacking faults are created perpendicular to the growth direction of the nanorod, especially at the interface of the particles, to release the strain and further maintain the unriped rodlike structure (Figure 3e). Besides the stacking faults, the interior strain in the nanorod is released by creating distortion and dislocations in the orientation of the (0001) crystal planes (Figure 3f). Furthermore, the grain boundaries between the ZnO particles are observed and, for example, indicated by 1 shown in Figure 3g. The microscopic grain boundaries and structural faults are indicative of crystal formation via association/attachment of nanoparticles.

Raman spectroscopy is also performed to study the crystallization degree of the flowerlike ZnO nanorod bundles. It is well-known that hexagonal ZnO has characteristic Raman peaks due to  $C_{6v}$  symmetry. Single-crystalline wurtzite ZnO has eight sets of optical phonon modes at the  $\Gamma$  point of the Brillouin zone, in which the  $A_1 + E_1 + 2E_2$  modes show Raman activity. In addition,  $A_1$  and  $E_1$  modes split into longitudinal (LO) and transverse (TO) optical components.<sup>21</sup> The  $E_2$  modes consist of two modes of low- and high-frequency phonons. Figure 4 shows the room temperature Raman spectrum of the ZnO products at the range of 200–800  $\text{cm}^{-1}$ . All observed spectral peaks could be assigned to wurtzite ZnO structure according to the literature values.<sup>21</sup> The dominant feature around 438  $\text{cm}^{-1}$  is due to ZnO nonpolar optical phonons  $E_2(\text{high})$  mode, which is a typical Raman peak of bulk ZnO crystal. It is very intense and the full width at half-maximum of peak is 15  $\text{cm}^{-1}$ . The asymmetrical and line-broadening characteristics mask  $E_1(\text{TO})$ , which is not obvious and peaks at 410  $\text{cm}^{-1}$  on the left-hand side of  $E_2(\text{high})$ . The appearance of the longitudinal optical at 579  $\text{cm}^{-1}$  is attributed to the  $E_1(\text{LO})$  mode, which is caused by the formation

of defects such as oxygen vacancy or other defect states.<sup>22</sup> According to the FESEM and TEM results, the large surface area and high surface roughness imply the pronounced enhancement of surface activity compared with that of bulk crystals, which may activate the normally forbidden  $E_1(\text{LO})$  mode. In addition, the peaks at 380 and 541  $\text{cm}^{-1}$  correspond to  $A_1(\text{TO})$  and  $A_1(\text{LO})$  phonons, respectively. Other relatively high peaks located at 331 and 662  $\text{cm}^{-1}$  cannot be explained within the framework of the bulk phonon modes, which may be attributed to multiphonon scattering process and assigned to  $3E_{2H}-E_{2L}$  and  $2(E_{2H}-E_{2L})$  modes, respectively.<sup>23</sup>

PEG plays an important role in obtaining the novel flowerlike ZnO nanostructures composed of numerous tiny nanoparticles. To actually understand the effect of PEG on the flowerlike ZnO nanostructures, the controlled experiment of hydrothermal process without PEG is carried out. Figure 5 shows the FESEM image of the ZnO products prepared by the hydrothermal route without PEG. It shows that only ZnO nanoparticles with average diameter of 80 nm are formed, and the results reveal that without PEG there is not enough driving force to grow the flowerlike ZnO nanorod bundles.

**Growth Process and Mechanism.** It is well-known that ZnO is a polar crystal exhibiting a basal positive polar plane (0001) and a negative polar plane (000 $\bar{1}$ ), which are rich in Zn and O, respectively. These polar planes with surface dipoles are thermodynamically unstable and have higher growth rate to reduce their surface energy.<sup>24</sup> In the aqueous solution system, the growth unit of  $[\text{Zn}(\text{OH})_4]^{2-}$  prefers to be adsorbed on the positive polar plane (0001) by relatively strong electrostatic attraction,<sup>25</sup> resulting in faster growth along the [0001] direction. In the surfactant-assisted hydrothermal process, the complexing agents are formed and have the ability to restrict the growth on some specific crystal planes to control the shape and size of the ZnO samples.<sup>26</sup>

Based on the basis of the investigations described above and the experimental results, a possible formation process demon-



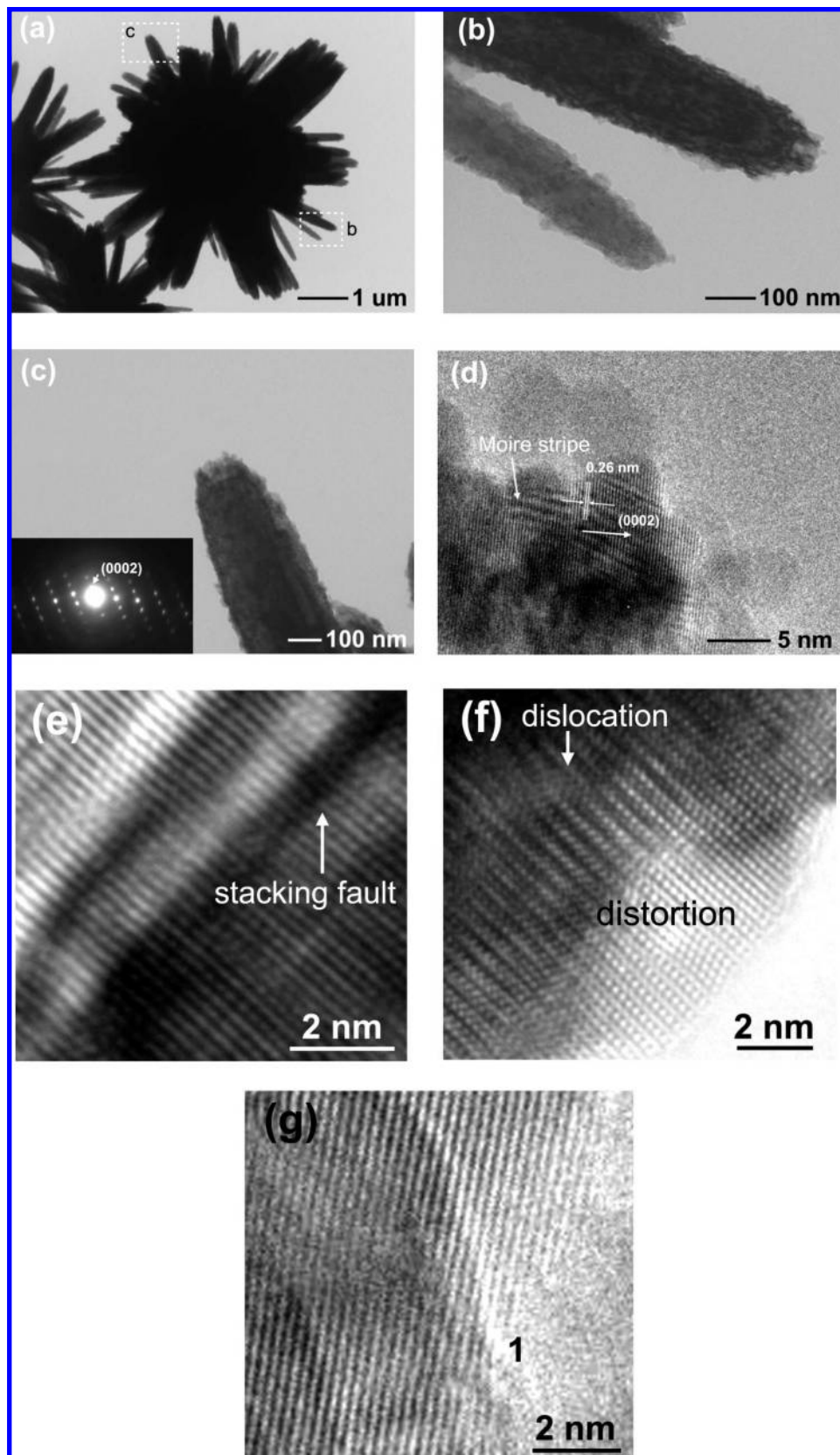


**Figure 3.** (a) TEM image of the typical flowerlike ZnO nanorod bundles. (b,c) Enlarged images of the connecting area labeled by rectangles in Figure 3a, respectively. The inset of Figure 3c is the corresponding SAED pattern. (d) HRTEM image of the tip of a selected typical ZnO nanorod. (e–g) Enlarged local images of ZnO nanorods showing the structural faults in the self-assembled process.

strating the synthesis of the present ZnO nanostructures can be explained in Figure 6. First, when ammonia solution is introduced into  $\text{Zn}^{2+}$  aqueous solution ( $\text{pH} < 10$ ) without PEG, the aqueous solution exhibits a frosty color due to the formation

of  $\text{Zn}(\text{OH})_2$  colloids. The formed  $\text{Zn}(\text{OH})_2$  could dissolve to a considerable extent into  $\text{Zn}^{2+}$  and  $\text{OH}^-$  ions in the hydrothermal process. When the concentration of  $\text{Zn}^{2+}$  and  $\text{OH}^-$  ions exceeds the critical value, the ZnO nuclei are formed. However, the

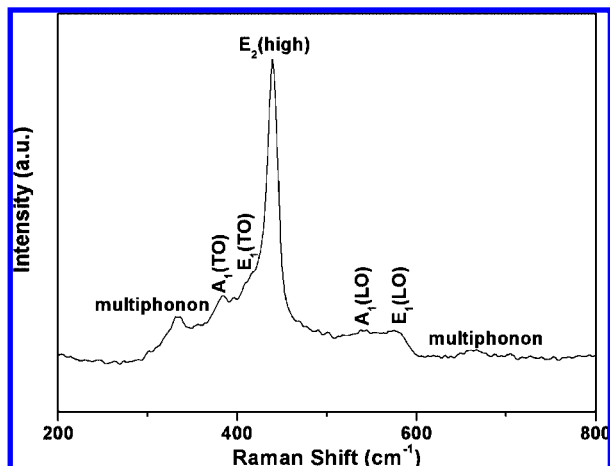


**Figure 4.** Room-temperature Raman spectrum of the flowerlike ZnO nanorod bundles.

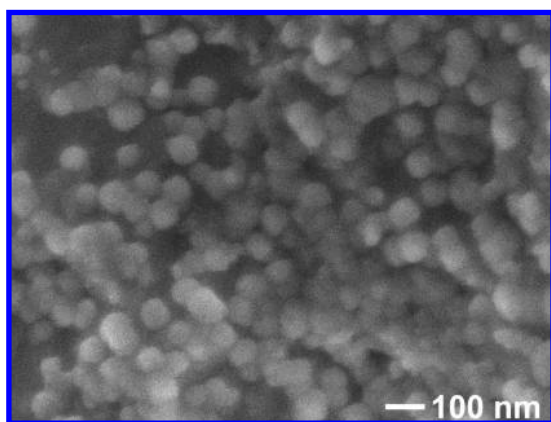


**Figure 5.** FESEM image of the ZnO products without PEG.

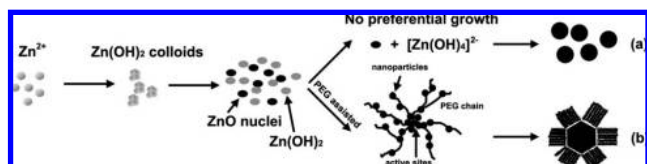


**Figure 6.** Growth schematic diagram of the ZnO products by the hydrothermal process with and without the PEG.

quantity of the growth unit of  $[\text{Zn}(\text{OH})_4]^{2-}$  is not enough and the growth of the ZnO nuclei are restrained. Thus, there are only ZnO nanoparticles obtained (Figure 6a). On the other hand, in the PEG-assisted hydrothermal process (Figure 6b), due to the water-soluble long flexural chain, large quantities of ZnO nuclei are adsorbed easily on these surfaces.<sup>27</sup> Under the Coulomb force interaction between the  $\text{Zn}^{2+}$  and O atoms in the chain of C—O—C, the ZnO nuclei can be formed preferentially on the coalescent sites. At further stage, the growth on certain specific crystal planes of the ZnO nanoparticles is restricted due to the strong binding linked selectively with PEG molecules.<sup>28</sup> On the surface of the active sites, the radial accumulation of the ZnO nanoparticles forms the rodlike shape. With further rotation of adjacent nanoparticles to share the same 3D crystallographic orientation and subsequent coalescence among these nanoparticles, the loose rodlike structures are formed. Finally, the loose aggregates further crystallize and become compact gradually through Ostwald ripening to reduce the interfacial energy.

**Optical Properties Measurement.** UV-vis absorption and PL spectra are carried out to evaluate the crystallization degree

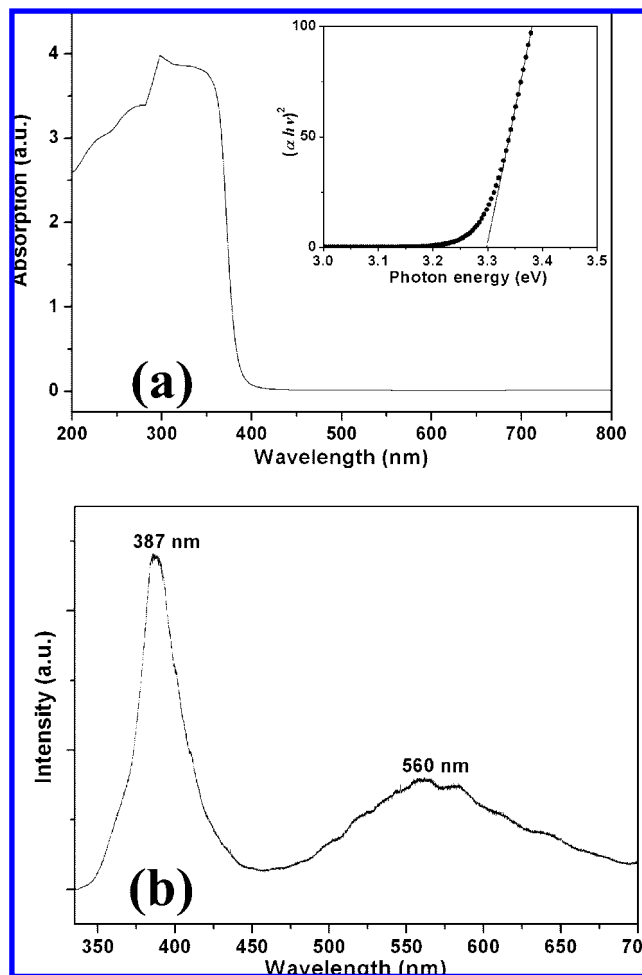


**Figure 7.** (a) UV-vis absorption spectrum and (b) room-temperature PL spectrum of the flowerlike ZnO nanorod bundles. The inset in (a) shows the corresponding plot of  $(\alpha h\nu)^2$  vs photon energy.

and the potential optical properties of the as-prepared ZnO products. As the size of the ZnO nanostructures is too large (larger than the half-wavelength), the UV-vis absorption spectrum consists of absorption and reflection due to the particle characteristics of light, and the UV-vis spectrum obtained from the suspension of the powder sample is not reasonable. Therefore, the absorption spectrum can be obtained by the measurement of the ZnO samples in the reflection mode. After the conversion, the absorption spectrum is shown in Figure 7a. The peak in the spectrum is due to the change of the light source at the wavelength of about 298 nm. The band gap energy  $E_g$  for the ZnO samples can be determined by extrapolation to the zero absorption coefficient.<sup>29</sup> As shown in the inset of Figure 7a, the intercept of the tangent to the plot will give a good approximation of the band gap energy for this direct band gap material. Extrapolation of linear portion to the energy axis at  $(\alpha h\nu)^2 = 0$  gives the  $E_g$  value. The band gap of 3.298 eV for the as-prepared ZnO samples is almost in accordance with the value of the bulk ZnO.<sup>29c</sup>

As shown in Figure 7b, the room temperature PL spectrum recorded from the present flowerlike ZnO products displays an intensive UV emission peak at ~387 nm and a relatively weak and broad green-yellow emission peak at ~560 nm. It is well-known that the UV emission peak usually originates from the near band-edge emission of the wide band gap from the recombination of the free excitons.<sup>30</sup> It is generally accepted that the impurities and structural defects, such as oxygen

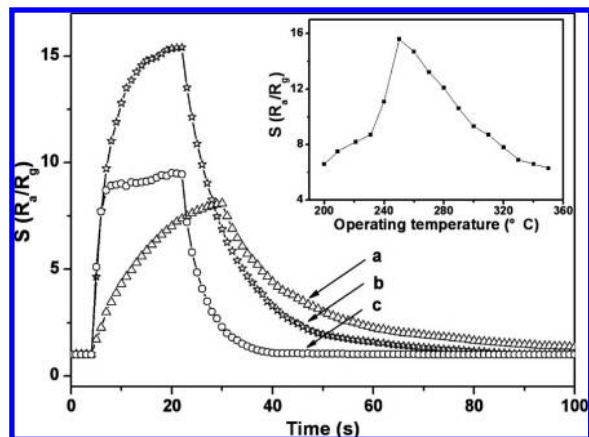


**Figure 8.** Response of the present ZnO to 10 ppm ethanol at various operating temperatures of (a) 220, (b) 250, and (c) 300 °C, respectively. The inset shows the sensitivity to 10 ppm ethanol at the operating temperature in the range of 200–350 °C.

vacancies, are responsible for the deep level or trap-state emission in the visible range.<sup>30b,31</sup> The green-yellow emission broadband centered at about 560 nm is considered to be the result from radiative recombination of a photon-generated hole with an electron occupying the oxygen vacancy.<sup>30</sup> In our work, the green-yellow emission is not negligible compared with the relatively intensive UV emission. It indicates that there are many oxygen vacancies or structural defects in the ZnO self-assembled nanorods, which is in good agreement with the HRTEM and Raman results. As for the application of the present ZnO to gas sensors, the high oxygen vacancies are beneficial, which can increase the electrostatic interaction between the gas molecules and the surface of ZnO nanorods.

**Gas-Sensing Properties.** The gas-sensing properties of the ZnO nanorod bundles are measured at various operating temperatures and ethanol concentrations. Considering the purposes of the optimal sensitive characteristics and the practical applications of the novel ZnO nanostructures, the effect of operating temperature is first studied at the fixed ethanol concentration of 10 ppm. Figure 8 shows the typical response curves of the present ZnO to 10 ppm ethanol for a period of time at the operating temperature of 220, 250, and 300 °C, respectively. The sensitivity and response–recovery time of the present ZnO are significantly different at different given operating temperatures. Among these response curves, the maximum sensitive value is about 15.6 at the operating temperature of 250 °C. Furthermore, the response and recovery times are clearly found to decrease with increasing the operating temperature from 200 to 350 °C. It can be explained from the kinetics and mechanics of the gas adsorption and desorption on the surface of ZnO or other similar semiconducting metal oxides.<sup>32</sup> It is observed in the inset of Figure 8 that the sensitivities of the present ZnO are found to increase on increasing the operating temperature, attain the maximum, and then decrease on further increasing the operating temperature. The maximum response value of 15.6 is obtained at the operating temperature of 250 °C, which is lower than the results of the literature.<sup>33,34</sup> Thus, the ZnO nanorod bundles are very promising for fabricating gas sensors with the low-power consumption and fast response. Although the sensor can also be performed at the operating temperature as low as 140 °C, the potential applications, such as rapid and continuous detection, are limited due to the longer response time (>40 s). It is considered from the practical application that 250 °C is the optimum operating temperature for both relatively faster re-

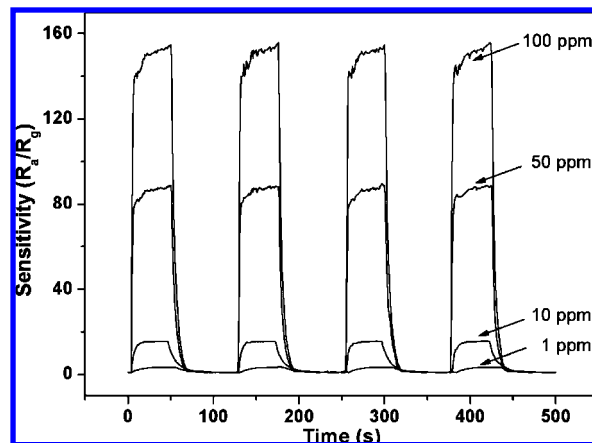
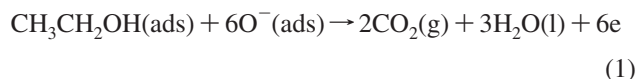


**Figure 9.** Response of the flowerlike ZnO nanorod bundles versus time to different ethanol concentrations at 250 °C.

sponse time and the highest sensitivity, and further sensing experiments are operated at 250 °C.

Figure 9 shows the response curve of the sensors to various ethanol concentrations at 250 °C. In the measurements, four periods are examined at each fixed concentration. The sensitivities are about 3.5, 15.6, 87.8, and 154.3 to 1, 10, 50, and 100 ppm ethanol, respectively. These results reveal that the sensors can detect ethanol vapor of concentrations down to 1 ppm. And it also can be obtained that the signal from the sensors becomes stable within 12 s after it is exposed to ethanol, and returns to the original values within 35 s after the tested target gas is replaced by air. Thus, the response time and recovery time are found to be about 12 and 35 s, respectively. Furthermore, good repeatability has been realized among the four cycles, which demonstrates the chemical stability of the sensors.

It is well-known that the sensitivity of semiconducting oxide gas sensor is determined by the resistance change, which is primarily controlled by the species and amount of chemisorbed oxygen ions ( $O^-$ ,  $O_2^-$ ,  $O^{2-}$ ) on the surface.<sup>35</sup> When the present ZnO is exposed to air atmosphere, oxygen molecules could be adsorbed on the ZnO surface and capture free electrons from them to form oxygen ions. Thus, the equilibration of the chemisorption process results in the formation of depletion layers on the surface regions and eventually increases the resistance of the sample. When ZnO is exposed to the target gas, these molecules could react with the oxygen ions adsorbed on the surface and release the trapped electrons back to the conduction band, as in eq 1, resulting in the increase of the conductivity. Therefore, it is undoubted that oxygen adsorption at air atmosphere is very important for the performance of the sensor. It can be concluded that the sensing materials with higher surface-to-volume ratio can adsorb more oxygen molecules, thus resulting in a higher sensitivity. The surface-to-volume ratios of the flowerlike ZnO nanorod bundles and ZnO nanoparticles fabricated without PEG are characterized by BET analysis using nitrogen adsorption. The BET surface areas of the flowerlike ZnO nanorods and ZnO nanoparticles are about 65.8 and 42.6  $m^2 g^{-1}$ , respectively, which indicate that the surface of flowerlike ZnO nanorod bundles can absorb more oxygen molecules.



The results of the sensitive testing show that the flowerlike ZnO nanorod bundles in the present work not only exhibit extremely high sensitivity but also can work at a relatively low



temperature. The enhancement in sensing properties of the present ZnO sensor may be attributed to the small grain size and high surface-to-volume ratio. The sensitivity is strongly dependent on the grain size and can be greatly increased when the grain size is comparable to the Debye length ( $L_d$ ).<sup>36</sup> In particular, even though the nanoparticles in the inner space of the nanorods are further crystallized to become integrated and share the same 3D crystallographic orientation, rough particle-assembled surfaces can still be observed. The peculiar nanoparticle-surface flowerlike morphology of ZnO not only provides a very coarse surface for efficient chemisorption due to the high surface-to-volume ratio but also leads to the insufficiency of surface atomic coordination and high surface energy, which can increase the surface activity and eventually promote further adsorption of oxygen.<sup>37</sup> On the other hand, the increased surface activity decreases the influence of the activation energies barrier. Therefore, at a relatively lower operating temperature, the target gas molecules have enough thermal energy to react with the adsorbed oxygen ions. In this case, at the operating temperature of 250 °C, the sensors exhibit satisfactory sensing properties and are very promising for the practical application.

#### 4. Conclusions

In summary, flowerlike ZnO nanorod bundles have been successfully synthesized by the PEG-assisted hydrothermal route at a low temperature without using any templates or substrates. The experimental results demonstrate that the formation of these self-assembled ZnO nanostructures composed of nanoparticles could be explained from the angle of nucleation and surfactant action. Sensors based on the flowerlike ZnO nanorod bundles exhibit high sensitivity to ethanol at 250 °C, which could be attributed to the high surface activity and surface-to-volume ratio. The testing results indicate that the present ZnO nanostructures are very promising for gas sensors with low power consumption.

**Acknowledgment.** We gratefully acknowledge financial support from the Science and Technology Office, Jilin Province, China (Granted No. 2006528) and the Open Project of Key Laboratory of Low Dimensional Materials & Application Technology (Xiangtan University), Ministry of Education, China (Granted No. KF0706).

#### References and Notes

- (1) Seiyama, T.; Kato, A.; Fujushi, K.; Nagatani, M. *Anal. Chem.* **1962**, *34*, 1502f.
- (2) Huang, M.; Mao, S.; Feick, H.; Yan, H.; Wu, Y.; Kind, H.; Weber, E.; Russo, R.; Yang, P. *Science* **2001**, *292*, 1897.
- (3) Kenanakis, G.; Vernardou, D.; Koudoumas, E.; Kiriakidis, G.; Katsarakis, N. *Sens. Actuators, B* **2007**, *124*, 187.
- (4) Chang, J. F.; Kuo, H. H.; Leu, I. C.; Hon, M. H. *Sens. Actuators, B* **2002**, *84*, 258.
- (5) Nanto, H.; Minami, T.; Takata, S. *J. Appl. Phys.* **1986**, *60* (2), 482.
- (6) Basu, S.; Dutta, A. *Sens. Actuators, B* **1994**, *22*, 83.
- (7) Shinde, V. R.; Gujar, T. P.; Lokhande, C. D. *Sens. Actuators, B* **2007**, *120*, 551.
- (8) Sberveglieri, G.; Baratto, C.; Comini, E.; Faglia, G.; Ferroni, M.; Ponzoni, A.; Vomiero, A. *Sens. Actuators, B* **2007**, *121*, 208.
- (9) Horrillo, M.; Gutierrez, J.; Ares, L.; Robla, J.; Sayago, I.; Getino, J.; Agapito, J. *Sens. Actuators, B* **1995**, *25*, 507.
- (10) Patil, D. R.; Patil, L. A. *Sens. Actuators, B* **2007**, *123*, 546.
- (11) Guo, L.; Ji, Y. L.; Xu, H. B.; Simon, P.; Wu, Z. Y. *J. Am. Chem. Soc.* **2002**, *124*, 14864.
- (12) Kong, X. Y.; Ding, Y.; Yang, R. S.; Wang, Z. L. *Science* **2004**, *303*, 1348.
- (13) Pan, Z. W.; Dai, Z. R.; Wang, Z. L. *Science* **2001**, *291*, 1947.
- (14) Yan, H. Q.; He, R. R.; Johnson, J.; Law, M.; Saykally, R. J.; Yang, P. D. *J. Am. Chem. Soc.* **2003**, *125*, 4728.
- (15) Yan, H.; He, R.; Pham, J.; Yang, P. D. *Adv. Mater.* **2003**, *15*, 402.
- (16) Peng, W. Q.; Qu, S. C.; Cong, G. W.; Wang, Z. G. *Cryst. Growth Des.* **2006**, *6*, 1518.
- (17) Feng, P.; Wan, Q.; Wang, T. H. *Appl. Phys. Lett.* **2005**, *87*, 213111.
- (18) Zhang, H.; Yang, D. R.; Ji, Y. J.; Ma, X. Y.; Xu, J.; Que, D. L. *J. Phys. Chem. B* **2004**, *108*, 3955.
- (19) Wang, J. X.; Sun, X. W.; Yang, Y.; Huang, H.; Lee, Y. C.; Tan, O. K.; Vayssieres, L. *Nanotechnology* **2006**, *17*, 4995.
- (20) Ge, J. P.; Wang, J.; Zhang, H. X.; Wang, X.; Peng, Q.; Li, Y. D. *Sens. Actuators, B* **2006**, *113*, 937.
- (21) Chen, S. J.; Liu, Y. C.; Shao, C. L.; Mu, R.; Lu, Y. M.; Zhang, J. Y.; Shen, D. Z.; Fan, X. W. *Adv. Mater.* **2005**, *17*, 586.
- (22) Pradhan, A. K.; Zhang, K.; Loutts, G. B.; Roy, U. N.; Cui, Y.; Burger, A. J. *Phys.: Condens. Matter* **2004**, *16*, 7123.
- (23) Damen, T. C.; Porto, S. P. S.; Tell, B. *Phys. Rev.* **1966**, *142*, 570.
- (24) Zhang, J.; Sun, L. D.; Yin, J. L.; Su, H. L.; Liao, C. S.; Yan, C. H. *Chem. Mater.* **2002**, *14*, 4172.
- (25) Govender, K.; Boyle, D. S.; Kenway, P. B.; O'Brien, P. J. *J. Mater. Chem.* **2004**, *14*, 2575.
- (26) Zhang, Z.; Sun, H.; Shao, X.; Li, D.; Yu, H.; Han, M. *Adv. Mater.* **2005**, *17*, 42.
- (27) Li, Z. Q.; Xiong, Y. J.; Xie, Y. *Inorg. Chem.* **2003**, *42*, 8105.
- (28) Gui, Z.; Liu, J.; Wang, Z.; Song, L.; Hu, Y.; Fan, W.; Chen, D. J. *Phys. Chem. B* **2005**, *109*, 1113.
- (29) (a) David, E. A.; Mott, N. F. *Philos. Mag.* **1970**, *22*, 903. (b) Tan, S. T.; Chen, B. J.; Sun, X. W.; Fan, W. J. *J. Appl. Phys.* **2005**, *98*, 013505. (c) Srikant, V.; Clarke, D. R. *J. Appl. Phys.* **1998**, *83*, 5447.
- (30) (a) Zhang, J.; Sun, L. D.; Liao, C. S.; Yang, C. H. *Chem. Commun.* **2002**, *3*, 262. (b) Chen, S. J.; Liu, Y. C.; Shao, C. L.; Mu, R.; Lu, Y. M.; Zhang, J. Y.; Shen, D. Z.; Fan, X. W. *Adv. Mater.* **2005**, *17*, 586.
- (31) Shen, G. Z.; Bando, Y.; Liu, B. D.; Golberg, D.; Lee, C. J. *Adv. Fuct. Mater.* **2006**, *16*, 410.
- (32) Yamazoe, N.; Fuchigami, J.; Kishikawa, M.; Seiyama, T. *Surf. Sci.* **1979**, *86*, 335.
- (33) Feng, P.; Wan, Q.; Wang, T. H. *Appl. Phys. Lett.* **2005**, *87*, 213111.
- (34) Wang, J. X.; Sun, X. W.; Yang, Y.; Huang, H.; Lee, Y. C.; Tan, O. K.; Vayssieres, L. *Nanotechnology* **2006**, *17*, 4995.
- (35) Gerigintschew, Z.; Forster, H.; Kositz, J.; Schipanski, D. *Sens. Actuators, B* **1995**, *26*, 170.
- (36) Geistlinger, H. *J. Appl. Phys.* **1996**, *80*, 1370.
- (37) Halperin, W. P. *Rev. Modern Phys.* **1986**, *58*, 533.